ABSTRACT

OPTICAL PROPERTIES OF SiGe NANOSTRUCTURES

by
Varun Sharma

In this thesis, Raman Scattering (RS) and photoluminescence (PL) measurements of Ge nanowires (NWs) grown via vapor-liquid-solid (VLS) using chemical vapor deposition silicon substrates consisting of (100) and (111) crystallographic orientations are reported. Ge NWs grown are ~40 nm in diameter, approximately a micrometer in length, and a sharp narrow Raman peak at ~300cm^{-1} indicates single crystal quality. An absence of SiGe peak in the Raman spectra indicates that SiGe interdiffusion is insignificant for the NW volume. Low temperature PL-intensity-dependence spectra indicate that the observed emission originates at the Ge NW – Si substrate interface, where SiGe intermixing has been detected. This interface is formed differently for (111) and (100) oriented Si substrates due to the <111> preferential growth direction of Ge NWs.

OPTICAL PROPERTIES OF SiGe NANOSTRUCTURES

by
Varun Sharma

A Thesis
Submitted to the Faculty of
New Jersey Institute of Technology
in Partial Fulfillment of the Requirements for the Degree of
Master of Science in Electrical Engineering

Department of Electrical and Computer Engineering

January 2005

Blank Page

APPROVAL PAGE

OPTICAL PROPERTIES OF SiGe NANOSTRUCTURES

Varun Sharma

Dr. Leonid Tsybeskov Thesis Advisor   Date
Associate Professor of Electrical and Computer Engineering, NJIT

Dr. Haim Grebel, Committee Member   Date
Professor of Electrical and Computer Engineering, NJIT

Dr. Marek Sosnowski, Committee Member   Date
Professor of Electrical and Computer Engineering, NJIT

BIOGRAPHICAL SKETCH

Author: Varun Sharma

Degree: Master of Science

Date: January 2005

Undergraduate and Graduate Education:

- Master of Science in Electrical Engineering,
  New Jersey Institute of Technology, Newark, NJ, 2005.

- Bachelor of Science in Physics,
  The Pennsylvania State University, University Park, PA, 2003.

Major: Electrical Engineering

Presentations and Publications

Boris Kamenev, Varun Sharma, Ted Kamins, Leonid Tsybeskov
       "Optical Properties of Ge Nanowires Grown on Silicon (100)
       And (111) Substrates," <u>Applied Physics Letters</u>, 2005.

Varun Sharma, Boris Kamenev, Ted Kamins, Leonid Tsybeskov
       "Optical Properties of Ge Nanowires Grown on Silicon (100)
       And (111) Substrates," <u>2004 MRS Meeting</u> in Boston, MA on
       Nov. 30th, 2004.

Dae-Yong Jeung, Varun Sharma, Qiming Zhang
       "Electro-Optic Properties of $Pb(Mg_{1/3}Nb_{2/3})$-$PiTiO_3$ Single
       Crystals at Compositions near the Morphotropic Phase Boundary,"
       <u>Japanese Journal of Applied Physics,</u> 82(2003), 4387-4389 .

To Didi, Mom, Daddy, and Kundan

ACKNOWLEDGMENT

I would like to express my thanks to Dr. Leonid Tsybeskov, who served as my research advisor, providing valuable insight, intuition, and constantly giving me support, and encouragement. Special thanks are given to Dr. Haim Grebel and Dr. Marek Sosnowski for taking the time to participate in my committee.

I would also like to thank Dr. Boris Kamenev for providing stimulating discussion and explanation.

I would like to especially thank my father, mother, and sister for providing support and motivation from day one. Finally, I would like to thank Kundan for challenging me daily.

TABLE OF CONTENTS

LIST OF FIGURES

CHAPTER 1

INTRODUCTION

High aspect ratio one-dimensional (1D) nanostructures or nanowires (NWs) are ideal systems for investigating the dependence of structural, electrical, optical and mechanical properties as a function of size and dimensionality. NWs are expected to play a major role in the future as active devices such as components in electrical and optical devices, and passive devices such as interconnects [1-7].

Important issues in the fabrication of NWs are their crystallographic order, and the substrate's influence. It is reported that Si and Ge NWs have a preferential <111> orientation along the growth direction [8-11]; similar to elongated Si nanocrystals fabricated via solid-phase crystallization [12]. Thus it is reasonable to presume that substrate orientation has an essential role in the formation of NW-substrate heterointerfaces, along with materials intermixing and local strain distribution. By using characterization techniques such as Optical Imaging, Raman scattering (RS) and photoluminescence (PL), information about the NW-substrate heterointerface can be obtained.

This thesis presents detailed studies of Ge NWs fabricated on Si (100) and Si (111) substrates using vapor-liquid-solid (VLS) growth. Background information is provided on the VLS growth method, imaging techniques, along with Raman scattering and photoluminescence techniques to support the conclusion that Ge NWs grown on both (100) and (111) Si substrates have significant differences, and SiGe intermixing plays a significant role in the initial stages of Ge NW growth.

CHAPTER 2

BACKGROUND

2.1 Vapor-Liquid-Solid and Other Mechanisms of NW Growth

An important matter in NWs is the assembly of atoms into a one-dimensional nanostructure in a both effective and controllable manner. In general, a prerequisite for a successful growth method is the ability to achieve nanometer scale control of the diameter during the anisotropic crystal growth phase while achieving exceptional crystallinity of the sample. In the past few years, various methods have been developed to create these 1D nanostructures namely template-directed synthesis, solution-liquid-solid (SLS), solvothermal, and vapor-liquid-solid (VLS). These diverse methods can be grouped into two major categories based on the reaction media which is used during the preparation: solution or gas phased.

Template-directed synthesis is a versatile method for constructing 1D nanostructures. In this method, the template serves as a framework against which materials with similar structure are synthesized. The templates consist of nanoscale channels within mesoporous materials, porous alumina and polycarbonate membranes, etc. The NWs which are produced are released from the templates by selective removal of the host matrix.
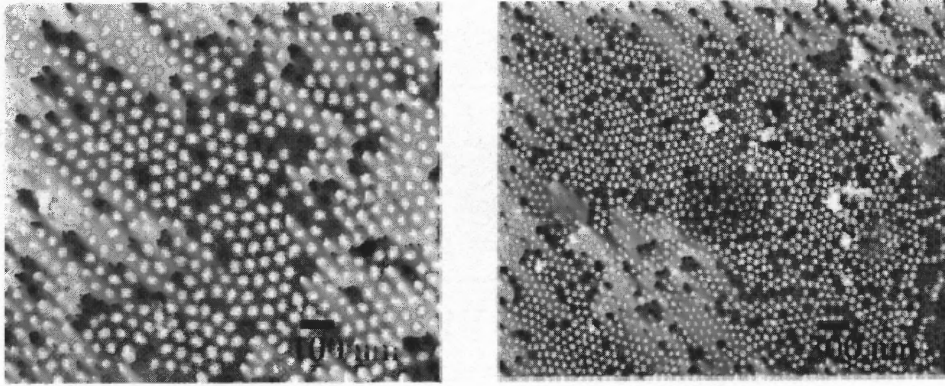
Figure 2.1 Scanning electron microscopy (SEM) image of Bi2Te3 nanowire array composite prepared using porous alumina as templates. The bright regions are the filled pores [23].

SLS growth method is used to obtain exceptionally crystalline NWs at low temperature. This method uses a low temperature phase reaction (203 ^{0}C or less). The resulting NWs are nearly single crystal, having widths of roughly 10 to 150 nanometers, and lengths consisting of several micrometers. Generally this method is used for the growth of InP, InAs, and GaAs nanowhiskers.
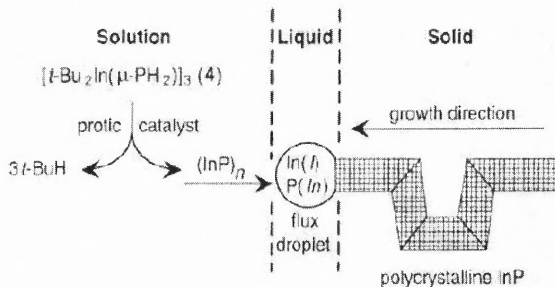
Figure 2.2 SLS growth mechanism [23].
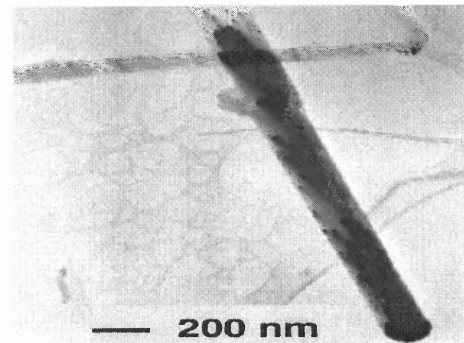
Figure 2.3 Al$_x$Ga$_{1-x}$As nanowhiskers grown by the SLS mechanism [23].

Solvothermal methodology has recently gained prominence as a possible method to the production of semiconductor nanorods and NWs. Here, a solvent is mixed with select metal precursors and a crystal growth regulator such as amines. The solution is

placed in an autoclave at high temperature and pressure for crystal growth and assembly to occur; resulting in various types of crystalline structures.
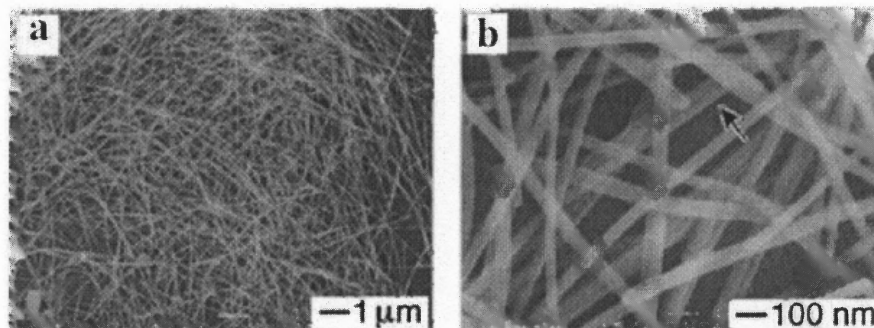
Figure 2.4 SEM images of Se nanowires that have a mean diameter of 32 nm and a standard deviation of 5 nm [19].

A well-accepted mechanism of nanowire growth via gas phase reaction is the vapor liquid solid (VLS) process proposed by Wagner in 1960 during his studies of large single-crystalline whisker growth [19]. According to this mechanism, the anisotropic crystal growth is promoted by the presence of liquid alloy/solid interface. The following diagram illustrates the growth of Ge NWs using Au clusters as a catalyst at high temperature.
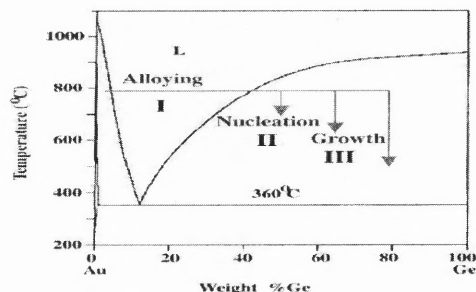
Figure 2.5 Au-Ge phase diagram showing three states along the isothermal line; (I) alloying, (II) nucleation, and (III) axial growth [20].

In VLS growth methodology, a metal particle is used as the catalytic nucleation site for the growth of NWs. Au, Fe, Ti, and Ga are generally used as the catalyst nanoparticle. The phase diagram previously presented allows the visualization of the eutectic temperature; NW growth temperature is generally set between the eutectic point and the melting point of the materials. The equilibrium melting point of a solid can be decreased though by decreasing the size of its particle due to the Gibbs-Thomson effect.

For an Au-Ge NW growth system, eutectic temperatures of $\sim 360^0$C allow for the low temperature synthesis of Ge NWs. It has been previously demonstrated that Au-Ge CVD by Au-catalyzed decomposition of GeH_4 source gas is possible even below the eutectic temperature [11]. At a given temperature, NWs grow, passing through the three states: alloying, nucleation, and growth. The chemical reaction that occurs can be expressed as:

$$GeH_4 \xrightarrow{Au} Au\text{-}Ge \text{ (l)} + 2H_2 \text{ (g)}.$$
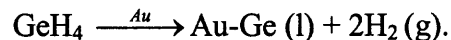
The growth mechanism for Au-catalyzed Ge NWs starts with the creation of a eutectic alloy between the Au particle and Ge. The Au particles are prepared by evaporating a Au film on to the Si substrate. The catalytic reaction then forms a thin, Ge rich layer on the surface of the Au-Ge particle at the growth end of the NW. The excess Ge at the surface results in a concentration gradient causing the excess Ge to diffuse throughout the Au-Ge island formed on the substrate.

This process can be further explained by the law of energy conservation. In order to form macroscopic quantities of Ge on the free surface of the Au-Ge alloy, an extra interface is formed increasing the overall energy of the system. If the excess Ge diffuses to the underlying particle – substrate interface, it can then attach to the Ge already present

without requiring an extra interface to form, conserving the total overall system energy [21].

As the Ge atoms precipitate on the underlying Ge, the Ge-Au island is forced upwards, forming the NW. Transport of the Ge from the alloy surface is done via bulk diffusion through the alloy particle, or surface diffusion on its surface. The following diagram is a schematical representation of Au-Ge NW growth on a Si substrate.
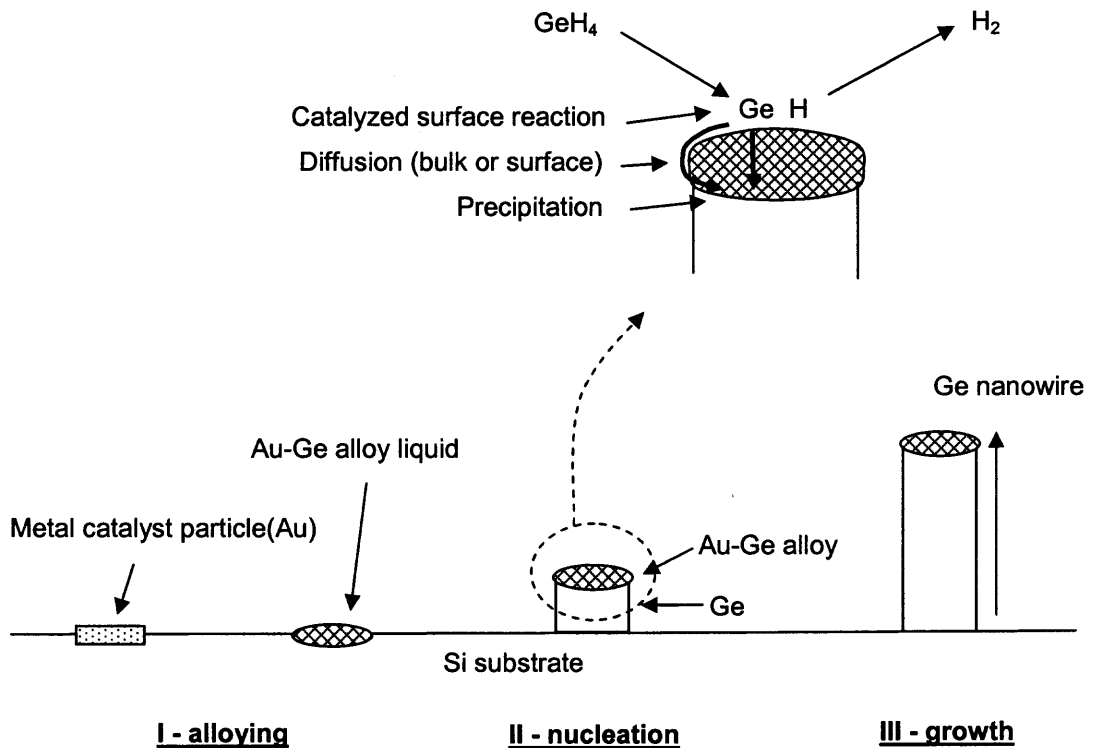
Figure 2.6 Schematical representation of Au-Ge NW growth on Si substrate.

The supersaturation and precipitation that occur on the growth interface depend on the diameter of the NW; Gibbs-Thomson equation places a lower limit on the diameter of structures for thermal growth [22]. The lower limit for the wire decreases with the

increase of gas pressure, therefore a higher gas pressure leads to an increase in the growth rate of the NW.

In order for the NW to grow, the transport of Ge must not be the limiting factor. If bulk or surface diffusion is slow, the Ge decomposing on the surface will cover the catalyst nanoparticles. As a result, the gas is unable to reach the particle, effectively destroying the growth system.
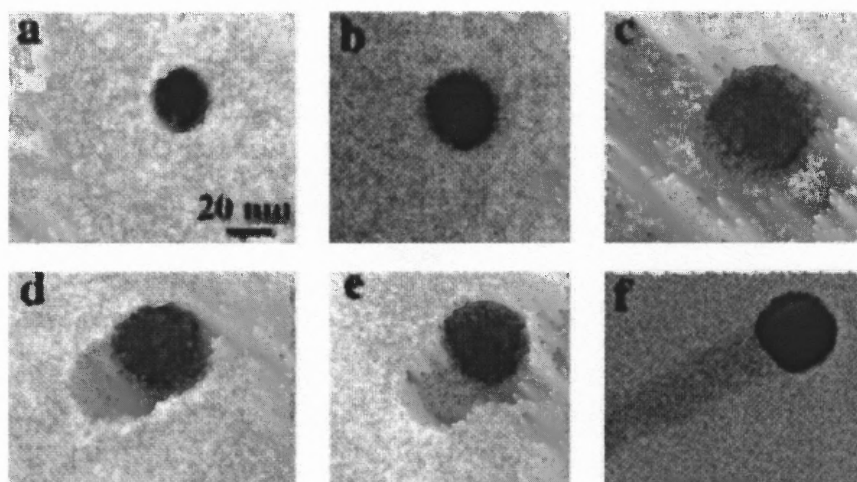
Figure 2.7 In situ TEM images recorded during the process of nanowire growth. (a) Au nanoclusters in solid state at 500^0 C; (b) alloying initiates at 800^0 C, at this stage Au exists mostly in solid state; (c) liquid Au/Ge alloy; (d) the nucleation of Ge nanocrystal on the alloy surface; (e) Ge nanocrystal elongates with further Ge condensation and eventually forms a wire (f) [23].

The image above shows the real time pictures of Ge NW growth taken by in situ high temperature TEM, corroborating with the methodology of the VLS growth mechanism [23]. The three previously discussed stages of growth (alloying, nucleation, axial growth) correlate to images (a)-(c), (d) and (e), and (f) respectively. Prior to the application of Ge vapor, the Au particles are in solid state. Once the amount of Ge vapor is increased across the surface of the nanoparticles, the Ge condenses and diffuses,

forming an alloy with the Au particle; eventually liquefying as the Ge content percentage increases in the alloy. Upon further inspection of images (a)-(c), it can be stated that increasing the size of the alloy droplet, and decreasing the contrast indicates that as the alloy composition changes with increasing Ge content, the droplet undergoes the transition from bi-phase region of solid Au and Au-Ge alloy, to a single phase region of Au-Ge liquid alloy. As the Ge content in the alloy increases, the precipitation of Ge after diffusion to the interface between the liquid alloy and solid causes NW nucleation (d). Once the Ge NW nucleates, transport of the Ge vapor into the system increases the Ge precipitation from the alloy (e), resulting in the upward growth to form the desired NW (f).

2.2 Structural Characterization

Structural characterization of NWs is performed by a combination of techniques; namely transmission electron microscopy (TEM), scanning electron microscopy (SEM), X-ray diffractometry (XRD), and electron diffractometry (ED). TEM and SEM are generally used to provide imaging of the desired structure, and XRD and ED assist in quantitative analysis.

Figure 2.8 (a) shows a high resolution transmission electron microscopy (HRTEM) image of a Si NW and (b) is a SEM image of a Ge NW grown via VLS. In the TEM image, it is apparent that the NW is of high crystallinity while the SEM image indicates an oxide layer surrounding the Ge NW.

(a)   (b)
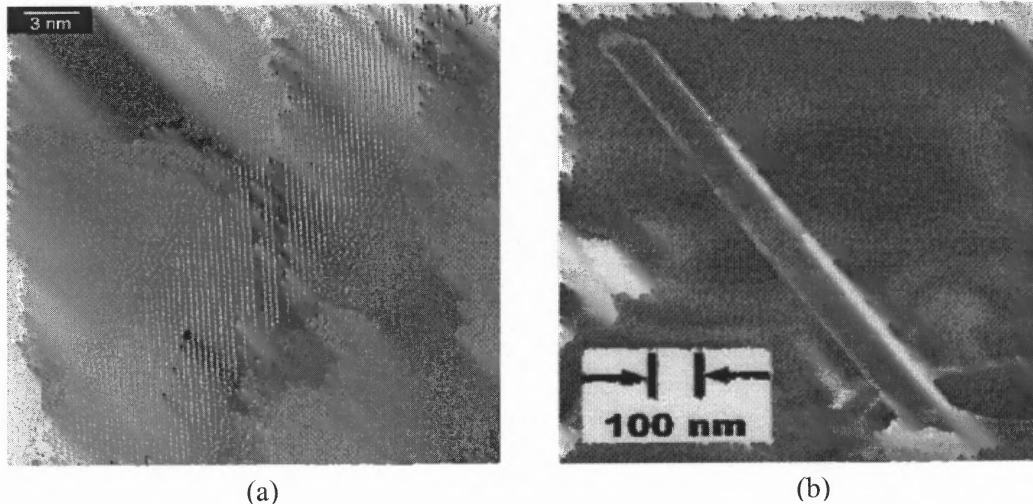
Figure 2.8 HRTEM image of Si NW (a) [22] and SEM image of Ge NW (b) [24].

Occasionally during NW growth, an amorphous snake like structure can form. If the source gas decomposition and diffusive transport on the catalyst nanoparticle is too rapid, the source material is supplied at a higher rate than the crystallization rate causing these structures [22]. The following TEM image (Figure 2.9 (a)) of Au-Si NWs grown via plasma enhanced CVD indicates that the increased growth rate, accommodated by RF plasma, causes the amorphous growth. Conversely, 3D nanorods may form if the decomposition rate is greater than the transport rate, low gas pressure, etc. as shown in (b) [25].

(a)   (b)
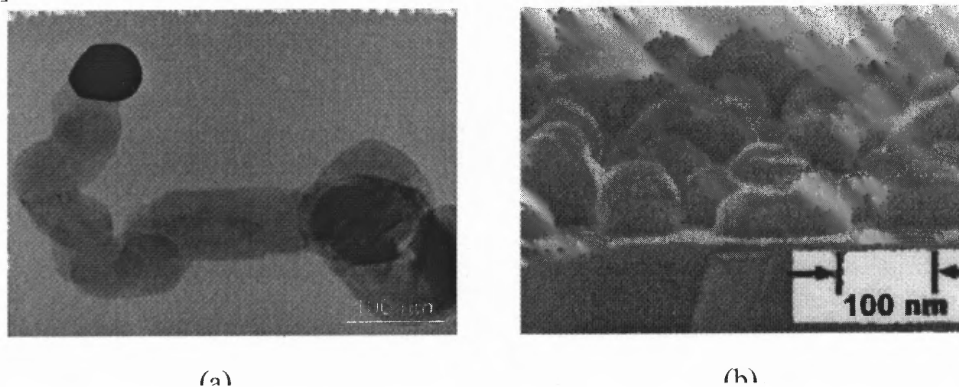
Figure 2.9 TEM image of amorphous Si NW (a) and SEM image of Ge nanorods (b) [25].

Kinks can occur in crystalline NWs, creating different crystal planes during growth [21] [24]. These kinks are generally due to twin dislocation defects. Twin dislocation defects form when a lattice mismatch between the catalyzing island and the NW is present [24]. In Figure 2.10 (a), a TEM image of a Si NW grown via MBE using $TiSi_2$ catalyst and Si_2H_6 gas source is presented. The strain from the inherent lattice mismatch of 6% between the Si NW and $TiSi_2$ island causes the formation of a twin crystal during the growth, in turn dominating the growth direction causing kinking. Figure 2.10 (b) shows a Si NW in which a twin crystal is developing at the lower edge while a Si crystal with stacking faults is forming at the upper edge. In the initial stage, the lattice stress at the heterointerface causes a Shockley partial dislocation at the edge of the $TiSi_2$ islands where the strain is the highest, and then propagates along the Si {111} plane. As the partial dislocation propagates through each parallel {111} plane, a twin crystal is formed; else a crystal full of stacking faults is formed. Once the twin is formed, it grows along the NW, eventually causing the NW to kink. The twinning process can occur multiple times during the course of NW growth, causing multiple changes in growth directions.
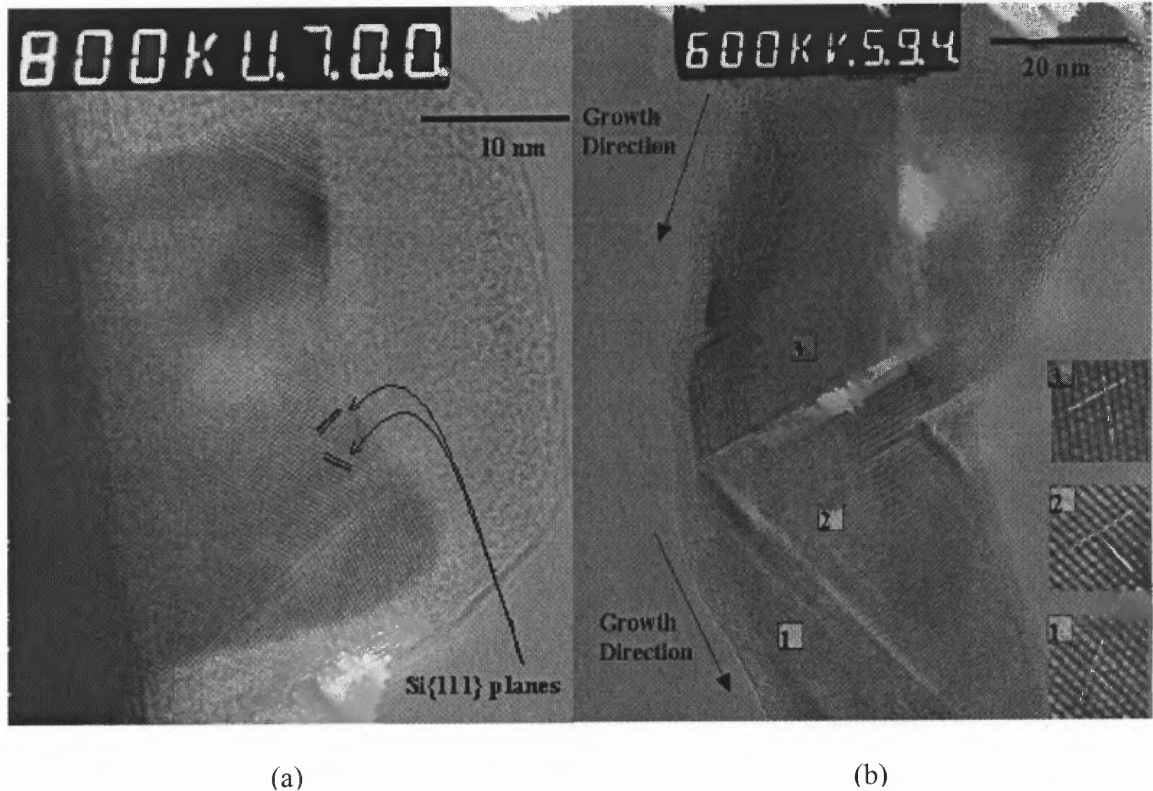
Figure 2.10 TEM image of Si NWs containing twin crystals. A short Si NW (a) and SI NW with kink (b). In (b), the insets are enlarged Si crystal images at positions 1, 2, and 3. The white lies correspond to (111) planes. Si lattice 1 is twin to 2, which is twin to 3 [24].

X-ray and electron diffraction can give complementary quantitative information to TEM and SEM imaging. Both X-ray and electron diffraction are quite useful tools because they allow direct identification of a crystalline materials based on their crystal structure.

In X-ray diffraction (XRD), the intensity of the diffracted X-rays are measured as a function of the material's orientation and the angle of diffraction. In Electron diffraction, the diffracted beams have an extremely high intensity along with an exposure time in the order of seconds allows for the direct viewing of patterns via electron microscope. Also, diffraction patters are obtainable from microscopic crystals via

Selected Area Electron Diffraction (SAED) and by focusing an electron beam from non-sized regions (Convergent Beam Electron Diffraction CBED).

Figure 2.11 presents an SAED pattern and XRD spectrum of Si NW arrays grown via CVD template method using an alumina template [26]. In the SAED image a single Si NW is used; diffraction spots are in a hexagon pattern indicating that the diamond lattice structure of bulk Si is preserved in the NWs; each NW is represented as a single crystal. The XRD results indicate a polycrystalline structure, conflicting with the SAED results. Taking into account it is statistical results collected via XRD, and the diffraction patterns indicate different orientations, it can be surmised that the individual Si NW are single crystal, the Si NW in an array have different crystallographic orientation.

(a)   (b)
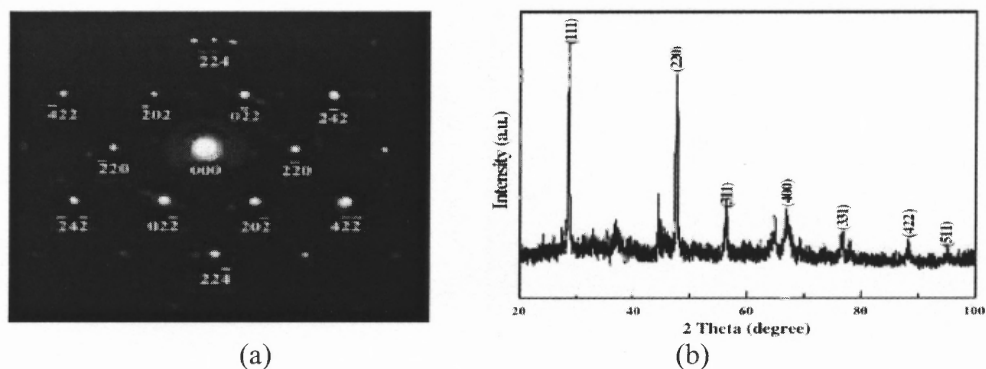
Figure 2.11 SAED pattern of a single Si NW (a) and XRD spectrum of Si NW arrays (b) [26].

2.3 Raman Scattering

The Raman effect was first discovered in 1928 by Sir Chandrasekhar Venkata Raman. In 1930, a Nobel Prize in Physics was awarded to him for his discovery and research of this phenomenon.

When light scatters, most photons are elastically scattered with the same frequency and wavelength as the incident photons. At random, a small fraction of light is scattered at frequencies generally lower than the frequencies of the incident photon. This occurrence of inelastic scattering is the Raman effect. Raman scattering occurs when there is a rotational, vibrational or electronic energy change of an atom.

The Raman effect occurs when a photon is incident on a given molecule and interacts with its electric dipole. In terms of classical physics, this interaction can be considered as a perturbation of the atom's E-field; whereas in quantum mechanics the interaction can be depicted as an excitation to a virtual state of lower energy than an electronic transition with a nearly coincident de-excitation and change in the vibrational energy. Figure 2.12 below illustrates the virtual state description of scattering.
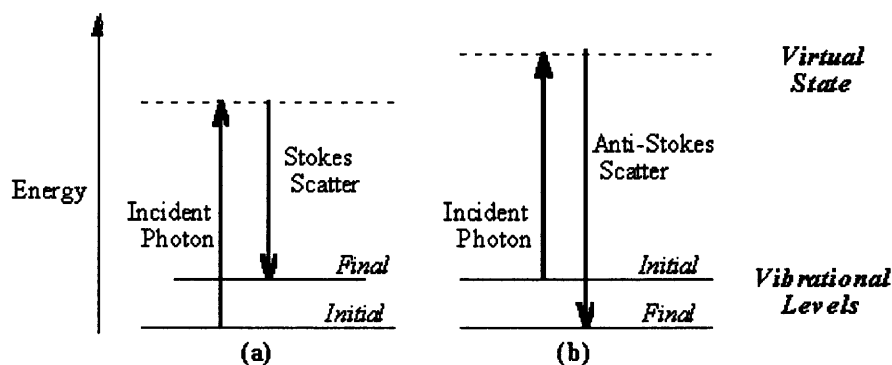
Figure 2.12 Energy level diagram for Raman scattering; Stokes region (a) and Anti-Stokes region (b).

The difference in energy between the scattered and incident photon is indicated by the arrows of different lengths as shown in Figure 2.12 (a). The numerical value of the energy difference, known as the Raman shift, can be calculated as:

$$Raman\ shift = \bar{v} = \frac{1}{\lambda_{incident}} - \frac{1}{\lambda_{scattered}}$$

Equation 2.1

$\lambda_{incident}$ and $\lambda_{scattered}$ are the wavelengths of the incident and scattered photons. The vibrational energy is dissipated as heat; due to the low intensity of Raman scattering, dissipated heat does not cause a rise in sample temperature.

Thermal population of vibrational excited states is low but not zero at room temperature. As a result, the ground state and scattered photon have a lower energy than the exciting photon. This phenomenon is known as the Stokes shift. A small percent of the atoms can be in vibrationally excited states and Raman scattering from vibrationally excited atom leave the atom in the ground state. The scattered photon will appear at a higher energy, known as the Anti-Stokes shift. The Anti-Stokes Raman spectrum is generally weaker than the Stokes spectrum, but is useful for detecting vibrational frequencies less than 1500 cm^{-1}. By taking the ratio of the Anti-Stokes intensity to the Stokes intensity, the sample temperature can be measured. Anti-Stokes measurements are most often used when the Stokes region is not easily observable due to various reasons such as poor spectrograph efficiency or detector response.

Vibrational spectroscopy of molecules can be quite complex. Quantum mechanics states that only well defined frequencies and atomic displacements are allowed. These states are the normal modes of vibration in a molecule. There are two types of molecules, linear and non-linear. A linear molecule made up of N atoms will have 3N - 5 normal modes, whereas a nonlinear molecule made up of N atoms will have 3N − 6 modes of vibration. There are various motions that can contribute to the normal mode: stretching motion between two bonded atoms, a bending motion between three

atoms which have two bonds, an out of plane deformation mode that can change a planar structure into a non planar, etc.

Infrared spectroscopy allows the characterization of vibrations in molecules by measuring light absorption at specific energies that correspond to the vibrational excitation of a molecule from a ground state to a higher state. Not all normal modes of vibration are excitable by infrared radiation; selection rules play a role in the ability of a molecule to be detected.

Through selection rules, it can be predicted if an observed vibration is Raman or infrared active. During the photon – molecule interaction, the overall angular momentum in the ground state must be conserved; therefore only certain transitions are possible. Molecular vibrations which are symmetric to the centre of symmetry are forbidden in the infrared region, while vibrations which are asymmetric to the center of symmetry are forbidden in the Raman region; this is mutual exclusion.

Infrared absorption is detectable if the dipole momentum (μ) changes during the normal vibration. The intensity of the infrared absorption band (I_{IR}) depends on the changing of μ during the vibration as indicated in the following equation:

$$I_{IR} \propto \left(\frac{\partial \mu}{\partial q} \right)_0^2$$

Equation 2.2

where q is the coordinate normal.

Active Raman vibrations are detectable if the polarizability (a) in a molecule changes during the normal vibration. The intensity of the Raman active band (I_{Raman}) depends on the changing of a during the vibration:

Equation 2.3

$$I_{Raman} \propto \left(\frac{\partial \alpha}{\partial q}\right)_0^2$$

Raman scattering is by default partially polarized in solids, and even liquids and gases where the individual molecules are randomly oriented. The polarization effect is easily visible with an excitation source which is plane polarized. In an isotropic media, polarization arises due to the fact that the induced electric dipole consists of components which vary spatially with respect to the coordinates of the molecule. Raman scattering from symmetric vibrations are strongly parallel polarized to the plane of polarization of the incident light. The scattered intensity from nonsymmetric vibrations will be ¾ as strong in the perpendicular plane of polarization of the incident light.

Polarization effects are even more complex when pertaining to crystalline materials. In this case, the crystal orientation is fixed in the optical system and the polarization component depends strongly on the crystal axes orientation with respect to the plane of polarization of the input light, along with the polarization of the input and observing polarizer.

Raman spectra are acquired by irradiating a given sample with a powerful laser source of visible or near-infrared monochromatic radiation. The choice of the laser line depends on the sample's materials and sometimes on the expected resonance profile of the Raman bands. Generally an Ar ion laser with output wavelengths in the green and blue region, or a Ar-Kr laser with an additional wavelength in the red region are used. The following diagram illustrates a basic Raman scattering setup. The laser is focused orthogonally on a given sample where the incident light scatters. The scattered light is

then measured via liquid cooled photomultiplier, and then outputted to a computer system.
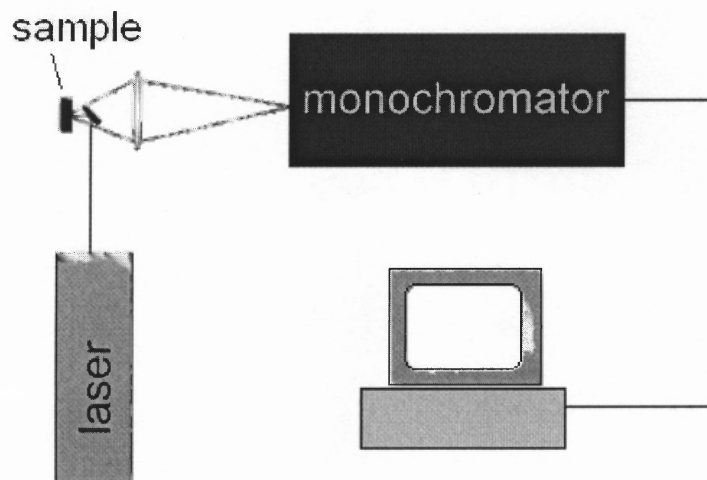
Figure 2.13 Block diagram of Raman scattering setup.

The Raman spectrum that is then displayed on the computer system is a plot of the intensity of the Raman scattered radiation as a function of its frequency difference from the incident radiation. The difference in frequency is the Raman shift and is generally measured in units of cm^{-1}; since this is a difference value, the Raman shift is not dependent of the frequency of the incident radiation.

Raman spectroscopy is an invaluable tool in the investigation of low energy excitations in various materials as well as in the characterization of their electronic, vibrational and structural properties. Figure 2.14 illustrates typical spectra in Si/SiGe nanostructures where three major modes (Si-Si, Si-Ge and Ge-Ge) are detected. In general, a shift in the Raman spectra positions, an increase in the full width of half maximum (FWHM), and the appearance of additional vibration modes (e.g., 505 and 450 cm^{-1}) indicate strain in 4.2% lattice mismatched SiGe epitaxial systems.
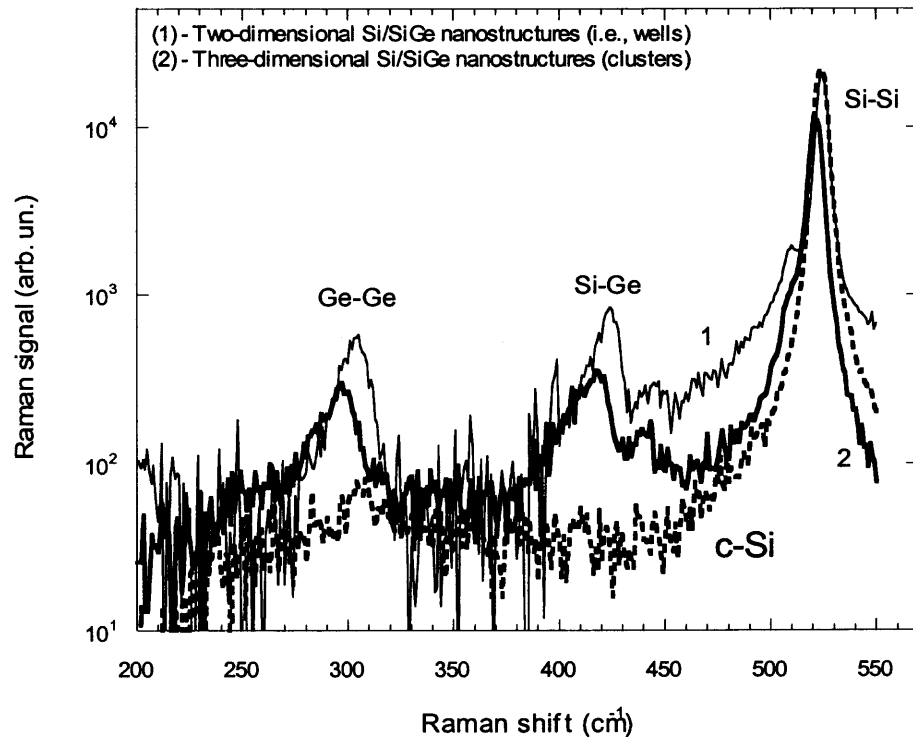
Figure 2.14 Typical spectra in Si/SiGe nanostructures where three major modes (Si-Si, Si-Ge and Ge-Ge) are detected. [27].

Figure 2.15 exemplifies a Raman spectrum of three-dimensional $Si/Si_{1-x}Ge_x$ nanostructures. The nanostructures are grown via molecular-beam epitaxy under conditions close to Stranski-Krastanov growth [27] with an excitation source consisting of an Ar+ laser (458 nm). The scattered light is analyzed using a JY 1 m double monochromater equipped with a liquid cooled photomultiplier and photon counting system.
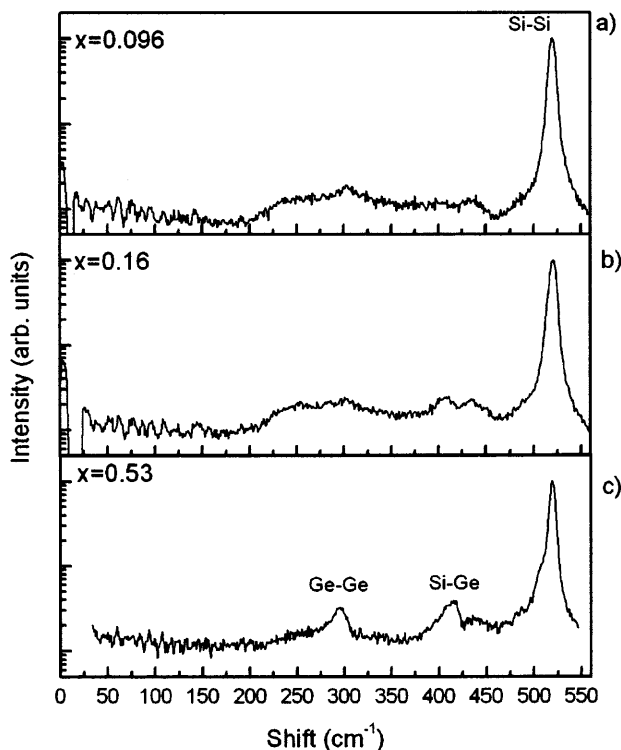
Figure 2.15 Raman spectra in 3D $Si/Si_{1-x}Ge_x$ nanostructures of different Ge content: (a) x=0.096; (b) x=0.16; (c) x=0.53 [27].

In $Si_{1-x}Ge_x$ clusters with low Ge content (x=0.096) (a), an optical phonon Raman signal related to the Si-Si vibrations with a main, zone-center phonon peak at ~520 cm^{-1} [28] and weak features at ~300 cm^{-1} related to Si acoustic phonons. No significant Raman peaks related to Ge-Ge vibrations at ~290 cm^{-1} and Si-Ge vibrations at ~420 cm^{-1} and to amorphous Si phase at ~480 cm^{-1} [29] were found.

Increasing the Ge content in the $Si_{1-x}Ge_x$ clusters up to x=0.16 (b) gives an increase in the intensity of the Raman peak that's associated with Si-Ge vibrations. The Raman peak related to Ge-Ge vibrations at ~290 cm^{-1} is still not visible.

Increasing the Ge content again to x=0.53 (c) in the $Si_{1-x}Ge_x$ clusters produces strong visible Raman peaks at ~ 290 cm^{-1} (Ge-Ge vibrations) and at ~420 cm^{-1} (Si-Ge vibrations).

2.4 Photoluminescence

All solids, including semiconductors, have so-called "energy gaps" for the conducting electrons. In order to understand the concept of a gap in energy, consider that some electrons in a solid are not firmly attached to the atoms, as they are for single atoms, but can move from one atom to another. The loosely attached electrons are bound in the solid by differing amounts and thus have much different energy. Electrons having energies above a certain value are referred to as conduction electrons, while electrons having energies below a certain value are referred to as valence electrons. This is shown in Figure 2.16 where they are labeled as conduction and valence bands.
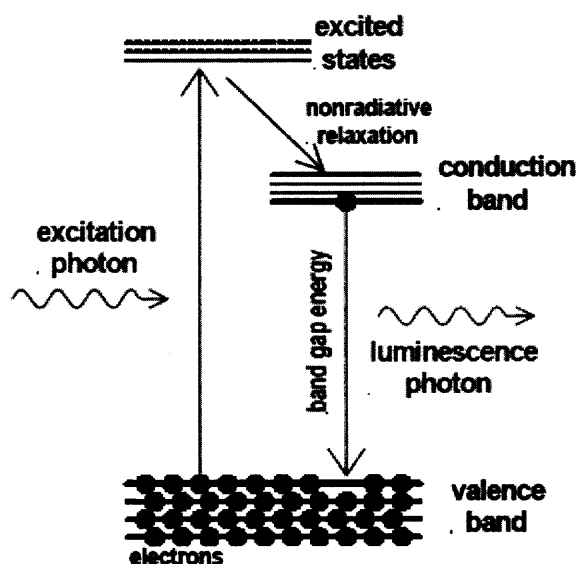

Figure 2.16 Schematical diagram of photoluminescence.

Furthermore, there is an energy gap between the conduction and valence electron states. Under normal conditions electrons are forbidden to have energies between the valence and conduction bands.

If a photon has energy greater than the band gap energy, then it can be absorbed and thereby raise an electron from the valence band up to the conduction band across the forbidden energy gap. In this process of photo excitation, the electron generally has excess energy which it loses before coming to rest at the lowest energy in the conduction band. At this point the electron eventually falls back down to the valence band. As it falls down, the energy it loses is converted back into a luminescent photon which is emitted from the material. Thus the energy of the emitted photon is a direct measure of the band gap energy, (E_g). The process of photon excitation followed by photon emission is called photoluminescence (PL).

In the bulk of crystalline materials, translational symmetry can cause the formation of energy bands. Impurities and defects can break the periodicity of the crystal lattice, causing perturbation to the band structure. This perturbation can be characterized by a specific energy level that lies within the bandgap. Contingent to the specific defect or impurity, the state can act as a donor or acceptor of excess electrons in the crystal. Electrons or holes can then be attracted to the excess or lack of local charge due to the impurity or defect, resulting in Coulomb binding. Since holes and electrons have different effective masses, acceptors and donors will have different binding energy.

Once the temperature is low enough, the carriers are trapped at these states. If the carriers undergo radiative recombination, the energy of the emitted light can be analyzed to determine the energy of the defect or impurity level. Shallow levels lying near the

conduction or valence band edge have a greater probability of participation in radiative recombination as long as the sample temperature is low enough to discourage thermal activation of carriers out of the traps. Deep levels often assist in nonradiative recombination by providing a stop for electrons that are moving between the conduction and valence bands by emitting phonons. Figure 2.17 illustrates radiative recombination paths consisting of band to band (a); donor to valence band (b); conduction band to acceptor (c); and nonradiative recombination through an intermediate state.
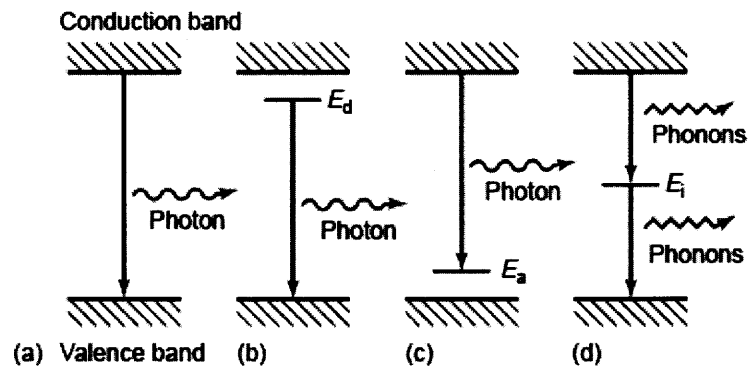
Figure 2.17 Radiative recombination states: band to band (a) donor to valence band (b) conduction band to acceptor (c); nonradiative recombination via intermediate acceptor (d).

PL emission favors sparse low-lying states due to the fact that photoexcited carriers rapidly thermalize throughout the bands and closely spaced state to within kT of the lowest available level. Because of this, PL is quite useful in the study of interfaces where specific defect and impurity states are present; if the specific state is radiative, it generates a peak in the PL spectrum.

Crystalline silicon is an indirect bandgap semiconductor, and this is perfectly illustrated by its photoluminescence spectra where phonon replicas are exhibited, proving

that electron-hole recombination in an indirect semiconductor requires phonons for momentum conservation as shown in Figure 2.18
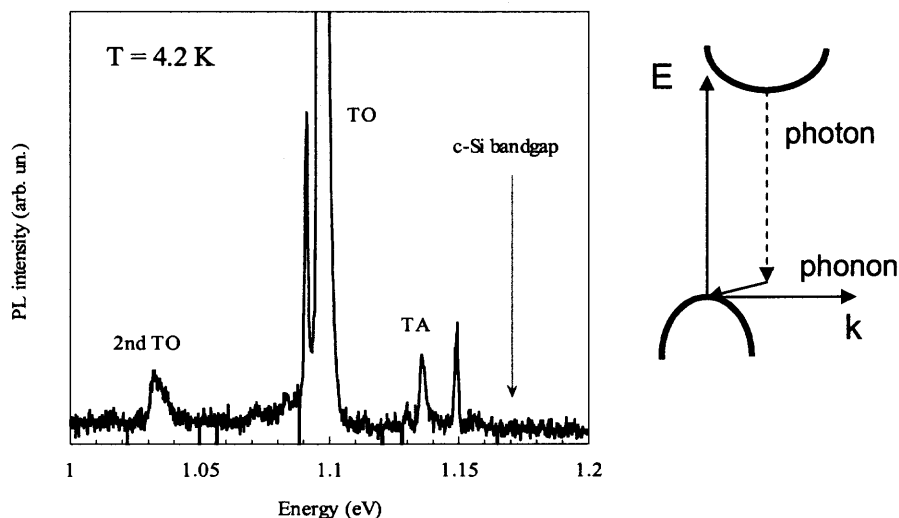
Figure 2.18 PL spectra of crystalline Si exhibiting phonon replicas [27].

PL peak positions can also be used to determine the composition of semiconductor alloys. The energy of the band-edge emission is correlated to the composition-dependant bandgap of the alloy; proving useful in interface analysis where interdiffusion can lead to interface alloying. Interface alloys form narrow wells that impact the characteristics of carriers at the heterojunction.

Referring back to the sample used in Raman spectroscopy measurements in Section 2.3, photoluminescence measurements can also be taken of this same sample; a typical PL setup is illustrated in Figure 2.19 The excitation source is again the same Ar laser (458 nm) used in Raman spectroscopy [27], with the excitation intensity varying from 0.1 to 10 W/cm^2. The PL signal is dispersed using a single grating Acton Research 0.5 m monochromater and detected via liquid N_2 InGaAs diode array in the spectral range

of 0.9-1.6 μm. The PL at longer wavelengths is measured using the same setup except

the InGaAs diode array has a spectral sensitivity of up to 2.6 μm. The measurements are

performed in a temperature range from 4 to 300 K.
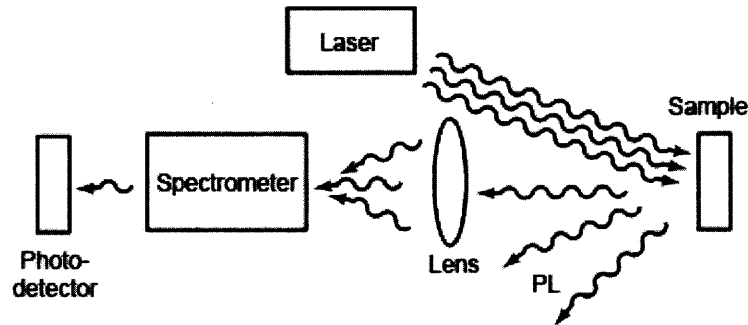
Figure 2.19 Typical photoluminescence setup.

The resulting PL spectra of samples consisting of Ge content from x=0.096 – 0.53 is

illustrated in Figure 2.20 In the $Si_{1-x}Ge_x$ nanoclusters with low Ge content (x=0.096), the

PL spectrum indicates that in addition to PL related to c-Si, PL bands at 1.05 and 1.11 eV

attributed to the no-phonon (NP) and TO phonon PL bands in Si-rich SiGe alloys are

observed (Figure 2.20 (a)) [27]. These PL bands are in the vicinity of c-Si luminescence,

and the intensities of the two PL bands are comparable, thus indicating that a small

amount of Ge (<10%) reduces the SiGe bandgap, relaxing the selection rules, and

increasing the ratio of NP/TO PL band intensities.

Increasing the Ge content within the nanoclusters to x=0.16 (Figure 2.20 (b))

changes the PL spectrum significantly. An intense PL band peaks at 0.95 eV indicating

an effective SiGe bandgap reduction of ~ 150 meV compared to that of c-Si. This broad

and featureless PL band with a full width at half-maximum of ~70 meV indicates a strong

compositional disorder compared to samples with x=0.096.

Further increasing the Ge content to x=0.53 in $Si_{1-x}Ge_x$ nanostructures gives a PL

spectrum depicting a broad double-peak feature with a major peak centered at 0.75 eV;

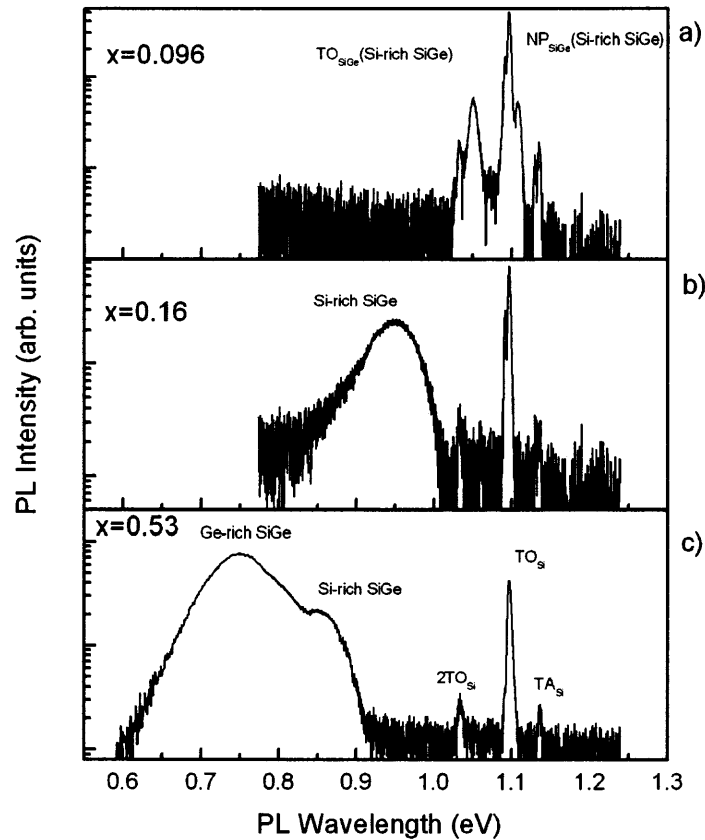close to the crystalline Ge (c-Ge) bandgap at 4 K [30]. A second PL peak is found at

~0.85 eV.

Figure 2.20 PL Spectra of $Si_{1-x}Ge_x$ at x=0.096 (a), x=0.16 (b), x=0.53 (c) [27].

CHAPTER 3

OPTICAL PROPERTIES OF Ge NANOWIRES GROWN
ON SILICON (100) AND (111) SUBSTRATES

3.1 Experimental Setup

The samples are grown via vapor-liquid-solid (VLS) technique using CVD of Ge with

pre-formed Au nanoparticles of 20 nm in diameter as the catalyst [11]. The nanoparticles

are deposited from an aqueous solution onto Si substrates with both (100) and (111)-4^0

crystal orientations. After inserting the substrates into a lamp-heated CVD reactor, they

are annealed in H_2 for 10 min at 650^0C in order to remove surface contamination from the

nanoparticles, and to alloy them with the Si substrates. The temperature is then reduced

to 320^0C and GeH_4 is introduced into the ambient H_2 in the process chamber. Deposition

times of 9, 18, and 36 minutes are used to form nanowires of different lengths; measured

to be 360, 710, and 1400 nm via scanning electron microscopy. The NWs are

simultaneously grown on both substrate orientations for each given deposition time in

order to minimize process variations, and to allow better comparison of the behavior of

both substrate orientations. The samples were finally cooled in H_2 and then N_2 to $<$

200^0C, minimizing oxidation; otherwise the Ge NW surfaces are not passivated. Figure

3.1 shows scanning-electron micrographs of Ge NWs grown on (100) and (111) single

crystal Si substrates. In each case, the Ge NWs (111) crystallographic growth orientation

determines the NW spatial growth direction. The majority of Ge NWs on a (100) Si

substrate form an angle of $\sim 55^0$ to the Si substrate, while on the (111) Si substrate they

grow nearly perpendicular to the substrate surface with a small inclination of $\sim 4^0$ (presumably due to the substrate surface cut-off).
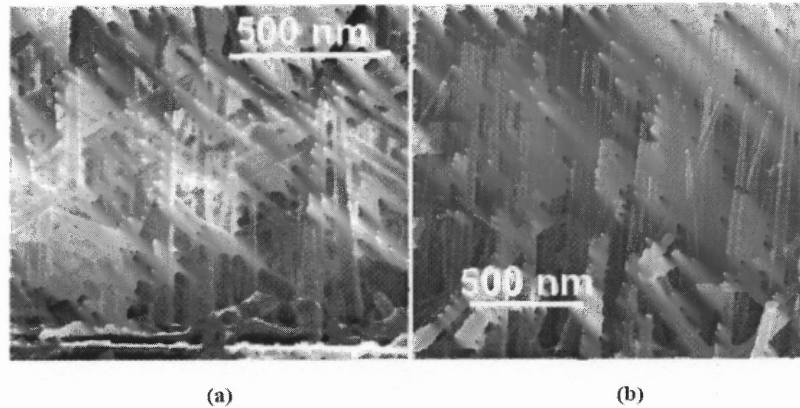
Figure 3.1 Scanning electron micrographs of Ge NWs grown on (a) (100) and (b) (111)-4° single-crystal Si substrates.

RS spectra are collected at room temperature in a backscattering geometry, using a 514nm line from an Ar^+ laser as the excitation source. The scattered light is analyzed using a JY one meter focal-length double monochromater equipped with a thermo-electrically cooled photomultiplier and a photon counting system.

For PL measurements, the excitation source is again a 514nm line from an Ar^+ laser with an excitation intensity of 0.1-$10W/cm^2$. The PL signal is dispersed using a single-grating Acton Research 0.5 meter focal-length monochromater, and detected by a liquid N_2 cooled InGaAs diode array in the spectral range of 0.9-1.6μm.

3.2 Results and Discussion

Figure 3.2 shows the Raman spectrum of Ge NWs grown on a (111) Si substrate in both the Anti-Stokes and Stokes regions. Two Raman peaks are clearly observed in both regions. The peak at ~ 520cm^{-1} is related to the Si-Si vibrations, and originates for the c-Si substrate. This has been verified using excitation sources of different wavelengths, along with samples of different Ge NW lengths. The peak at ~ 300cm^{-1} is related to Ge-Ge vibrations. The 300cm^{-1} Raman peak is fully symmetric with a full width at half maximum (FWHM) of ~ 6cm^{-1}; comparable to the Raman peak in single-crystal Ge [13, 14]. The narrow width of the NW Raman peak suggests that the Ge NWs are unstrained and of high crystalline quality. There are no significant SiGe vibrations found in the Raman measurements, indicating the NW substrate interface transition region is very thin. The Raman spectra are very similar for Ge NW samples grown on both (100) and (111) Si substrates.
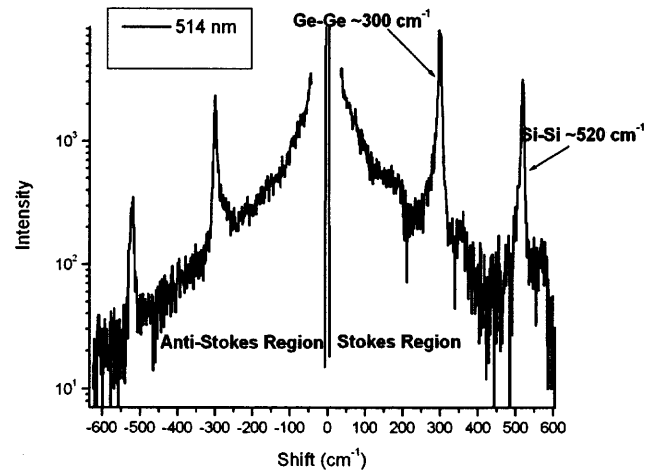

Figure 3.2 Raman spectra depicting Anti-Stokes and Stokes regions.

The ratio between Stokes and Anti-Stokes Raman peaks indicates insignificant sample heating by the laser beam using the relationship:

$$\frac{I_A}{I_S} = e^{-\frac{\hbar\omega}{kT}}$$

Equation 3.1

the sample temperature has been estimated. This is confirmed in Figure 3.3 where the

measured temperature vs. excitation photon energy is plotted; temperature remains

virtually constant through all excitation photon energies.
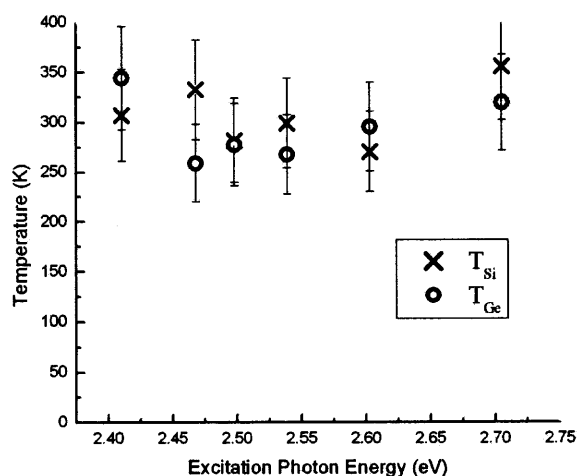
Figure 3.3 Temperature of Si and Ge.

Figures 3.4 and 3.5 are RS spectra of Ge NWs oriented on both (100) and (111) Si

substrates with excitation sources of 458nm and 514nm; focused about the Ge-Ge Raman

peak. It is clearly seen that under 458 nm excitation, the Raman peak is broader for Ge

NWs on (111) Si compared to Ge NWs on (100) Si. The Raman peaks under 514nm

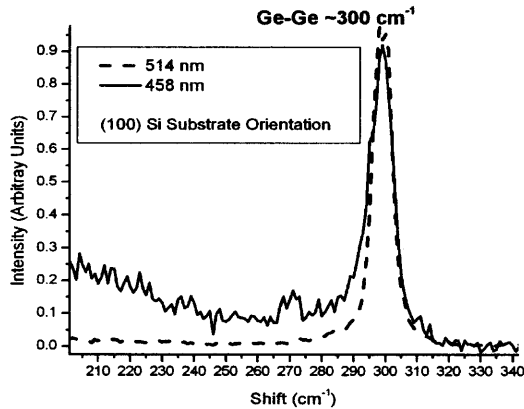excitation are similar for Ge NWs on both (100) and (111) Si orientation.

Figure 3.4 Raman spectra from the Ge NW sample grown on a (100) Si substrate with a NW length of 1400 nm.
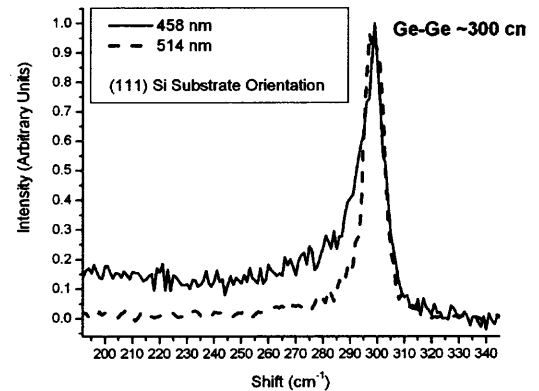
Figure 3.5 Raman spectra from the Ge NW sample grown on a (111) Si substrate with a NW length of 1400 nm.

Figure 3.6 compares the low-temperature PL spectra in single-crystal Si and in Ge NWs grown on (100) and (111) substrates. The main PL peak in Ge NWs (presumably the TO-phonon PL band) is slightly red-shifted compared to the PL spectrum of c-Si; ~20meV in Ge NW sample grown on Si(100), and ~45meV for Ge NWs grown on Si(111). The positions of the no-phonon PL lines, as well as TA_{Si} and $TO_{Si}+O(\Gamma)_{Si}$ phonons are also shown. Also, the ~20meV FWHM of the PL spectrum from the Ge NWs grown on the (111) Si substrate is roughly twice as broad as the FWHM of Ge NWs grown on the (100) substrate. Finally, the PL spectrum of Ge NWs grown on the (111) substrate display an additional feature at 1.074eV; possibly associated with one of the Si-Ge phonons [16].

Figure 3.6 Low-temperature PL spectra of c-Si and Ge NWs grown on (100) and (111) oriented Si substrates. The NP PL line and PL bands associated with characteristic phonons are shown.
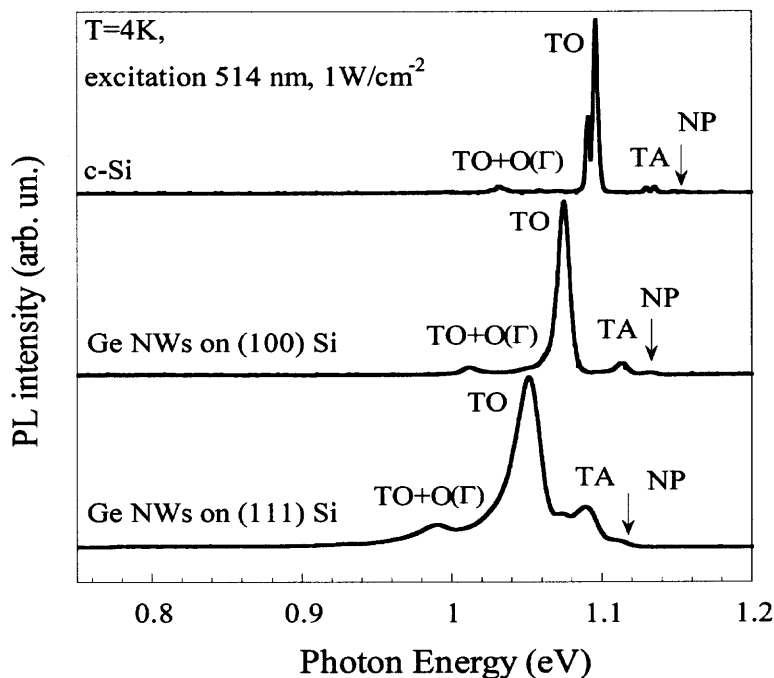
The data clearly suggests that the observed PL originates at the Ge NW – Si substrate heterointerface. First, the main PL peak is strongly blue shifted compared to the bandgap of crystalline Ge (~0.78 meV at 4 K). The blue shift does not result from any realistic value of axial strain, and the NWs average diameter of ~ 40nm is too large for any significant influence of quantum-confinement effects. It should be noted that similar spectra are also found in SiGe nanostructures with Ge content < 10% [17]. Second, the PL intensity shows no correlation with the NW length; it is similar for all three nanowire lengths and both substrates orientations used.

Why does the Ge NW volume not show a significant PL signal near the crystalline bandgap? Several reasons are possible; such as the relatively poor properties of Ge-Ge oxide interfaces with high concentrations of non-radiative recombination

centers, high NW surface-to-volume ratio, and possible incorporation of Au into the Ge

NW or on its surface during VLS growth. Since Au forms deep levels in crystalline Ge,

additional PL measurements in the IR region ($\lambda > 2.5\mu m$) are needed to verify the last

possibility.

The most fascinating result is the observed difference in the PL spectra between

samples grown on (111) and (100) substrates. A possible reason for this occurrence is the

PL arises from the NW – substrate interface region. The observation that the PL

spectrum from Ge NWs grown on (111) Si substrates is red shifted and broader compared

to the PL spectrum from NWs grown on (100) Si substrates indicates that SiGe

intermixing near the NW base is more efficient on samples grown on (111) Si substrates

regardless of an equal growth temperature ($T_G = 320^0 C$).

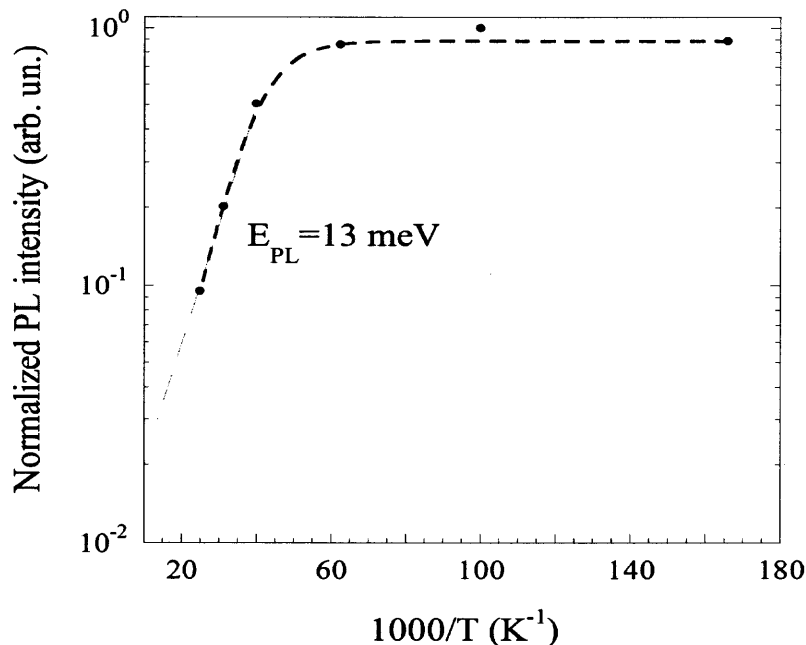**Figure 3.7** The PL intensity–temperature dependence in the sample with ~1.4 μm-long Ge NWs grown on a (100) Si substrate. The PL temperature dependence is similar for nanowires grown on (100) and (111) Si and for nanowires of different lengths.

The PL quantum efficiency is rather difficult to estimate due to the high surface scattering from the NW samples. The measurements indicate that Ge NWs grown on both (111) and (100) substrates have a PL external quantum efficiency of $\sim 10^{-2}\%$. The PL intensity does not depend on the NW length for either substrate orientations. The PL signal is temperature independent for T < 16K; decreasing exponentially with increasing temperature, exhibiting a PL thermal-quench activation energy of $E_{PL} \sim 13meV$ as shown in Figure 3.7. This activation energy is similar to the exciton binding energy in Si-rich SiGe alloys [16]. The polarization dependency of the PL intensity is found to be insignificant. A possible reason for the relatively low PL external quantum efficiency is the substrate interface transition region being quite thin, which is supported by the RS measurements.

CHAPTER 4

CONCLUSION AND FUTURE WORK

During the initial stage of VLS growth, Ge islands are formed in the area of the Si-Au nanoscale alloy droplets, creating NW bases [7-9]. Since Ge NWs have a preferential crystallographic growth direction, their bases and the NWs are perpendicular to a (111) Si substrate. In contrast, Ge NWs grown on (100) Si substrates are attached to the (111) facets of these initial Ge islands, resulting in most of the Ge NWs being inclined at $\sim 55^0$ to the Si substrate normal. Liquid-phase epitaxy is significantly different on Si (100) and Si (111), with different crystal structures initially forming [18], and possibly different initial rates of precipitation. Therefore, the different amounts of SiGe intermixing with the bases of the Ge NWs on different substrates can be attributed to the varying growth processes on the two crystallographic orientations, as well as possible differences in strain on the differently oriented substrates.

In conclusion, the RS and PL spectra presented indicate that Ge NWs grown on (111) and (100) crystalline Si substrates exhibit different amounts of SiGe intermixing near the NW – substrate interfaces. The results are especially important for devices utilizing novel, quasi one-dimensional heterojunctions at substrate – NW interfaces.

The measurements on Ge NW/Si substrate interface were inconclusive in the respect that heterojunction band discontinuities and deep states possibly exist in the germanium/germanium oxide interface; or from possible incorporation of Au particles during the Au-catalyzed CVD growth were not clearly investigated; further measurements will be needed to explore this area.

Future studies on these samples can be focused on several important issues namely: proper pasivation of Ge NW surfaces, most likely by Si, formation of Ge NWs embedded into a Si matrix, and time resolved photoconductivity under pulsed laser excitation.

This work presented in this thesis has been presented at the 2004 Fall MRS Convention in Boston, MA on November 30th, and has also been submitted as a paper to Applied Physics Letters.

REFERENCES

1. T. Ruecks, K. Kim, E. Joselevich, G. Y. Tseng, C. Cheung, C. M. Lieber, Science **289**, 94 (2000).

2. M. H. Huang, S. Mao, H. Feick, H. Yan, Y. Wu, H. Kind, E. Weber, R. Russo, P. Yang, Science **292**,1897 (2001).

3. A. M. Morales, C. M. Lieber, Science **279**, 208 (1998).

4. J. Yu, S. Chung, J. R. Heath, J. Phys. Chem. B **104**, 11864 (2000).

5. J. D. Holmes, K. P. Johnston, R. C. Doty, B. A. Korgel, Science **287**, 1471 (2000).

6. W. S. Shi, H. Y. Peng, Y. F. Zheng, N. Wang, N. G. Shang, Z. W. Pan, C. S. Lee, S. T. Lee, Adv. Mater. **12**, 1343 (2000).

7. T. I. Kamins, R. Stanley Williams, D. P. Basile, T. Hesjedal, and J. S. Harris, J. Appl. Phys. **89**, 1008 (2001).

8. Y. Wu, H. Yan, and P. Yang, Chemistry, Euro. J. **8**, 1260 (2002).

9. Y. Wu, H. Yan, and P. Yang, Topics in Catalysis **19**, 197 (2002).

10. J. Qi, J. M. White, A. M. Belcher, Y. Masumoto, Chemical Physics Letters **372**, 763 (2003).

11. T. I. Kamins, X. Li, R. Stanley Williams, and X. Liu, Nano Letters **4**, 503 (2004).

12. G. F. Grom, D. J. Lockwood, J. P. McCaffrey, H. J. Labbe, P. M. Fauchet, B. White Jr., J. Diener, D. Kovalev, F. Koch, L. Tsybeskov, Nature **407**, 358 (2000).

13. P. Y. Yu, M. Cardona, Fundamentals of Semiconductors: Physics and Materials Properties, Springer-Verlag, New York, 2001, pp. 617.

14. Z. Sui, H. H. Burke, I. P. Herman, Phys. Rev. B **48**, 2162 (1993).

15. G. Davies, Phys. Rep. **176**, 83 (1989).

16. J. Weber, M. I. Alonso, Phys. Rev. B **40**, 5683 (1989).

17. B. V. Kamenev, L. Tsybeskov, J.-M. Baribeau, D. J. Lockwood, Appl. Phys. Lett. **84**, 1293 (2004).

18. T. Füller, M. Konuma, J. Zipprich, and F. Banhart, Appl. Phys. A **69**, 597 (1999).

19. A. P. Levitt (ed.), *Whisker Technology*, Wiley-Interscience, New York (1970).

20. C. N. R. Rao, F. L. Deepak, Gautam Gundiah, and A. Govindaraj, Prog. Solid St. Chem. **31**, 5 (2003).

21. T. I. Kamins, R. Stanley Williams, D. P. Basile, T. Hesjedal, and J. S. Harris, J. Appl. Phys. **89**, 1008 (2001).

22. S. Hofmann, C, Ducati, R. J. Neill, S. Piscanec, A. C. Ferrari, J. Geng, R.E. Dunin-Borkowski, and J. Robertson, J. Appl. Phys. **94**, 6005 (2003).

23. Yiying Wu and Peidong Yang, J. Am. Chem. Soc. **123**, 3165 (2001).

24. Qiang Tang, Xian Liu, Theodore I. Kamins, Glenn S. Solomon, and James S. Harris, Appl. Phys. Lett. **81**, 2451 (2002).

25. J. L. Taraci, J.W. Dailey, T. Clement, David J. Smith, Jeff Drucker, and S. T. Picraux, Appl. Phys. Lett. **84**, 5302 (2004).

26. Mei Lu, Meng-Ke Li, Ling-Bing Kong, Xin-Yong Guo, and Hu-Lin Li, Composites: part B **35**, 179 (2004).

27. B. V. Kamenev, L. Tsybeskov, J.-M. Baribeau, D. J. Lockwood, Appl. Phys Lett. **84**, 1293 (2004)

28. Bibo Li, Dapeng Yu, and Shu-Lin Zhang, Phys. Rev. B **59**, 1645 (1999).

29. Li B, Yu D, and Zang SL., Phys. Rev. B **59**, 1645 (1999).

30. T. Baier, U. Mantz, K. Thonke, R. Saucer, R. Schäffler, and H. J. Herzog, Phys. Rev. B **50**, 15191 (1994).